Beginning of Activity in Long-period Comet C/2015 ER61 (PANSTARRS)

Karen J. Meech[1], Charles A. Schambeau[2], Kya Sorli[1,3], Jan T. Kleyna[1], Marco Micheli[4], James Bauer[5],
Larry Denneau[1], Jacqueline V. Keane[1], Elizabeth Toller[1], Richard Wainscoat[1], Olivier Hainaut[6],
Bhuwan Bhatt[7], Devendra Sahu[7], Bin Yang[8], Emily Kramer[5], and Gene Magnier[1]

[1] Institute for Astronomy, University of Hawai'i, 2680 Woodlawn Drive, Honolulu, HI 96822, USA
[2] University of Central Florida, Dept. of Physics, Physical Sciences Building, 430, Orlando, FL 32816-2385, USA
[3] Duke University, 401 Chapel Drive, Box 98062, Durham, NC 27708, USA
[4] ESA SSA-NEO Coordination Centre, Frascati, RM, Italy
[5] Jet Propulsion Laboratory, California Institute of Technology, 4800 Oak Grove Drive, MS 183-401, Pasadena CA 91109, USA
[6] European Southern Observatory, Karl-Schwarzschild-Strasse 2, D-85748 Garching bei Munchen, Germany
[7] Indian Institute of Astrophys., II Block, Koramangala, Bangalor 560 034, India
[8] European Southern Observatory, Álonso de Cordova 3107, Vitacura, Casilla 19001, Santiago, Chile

Abstract

We report the beginning of activity for comet C/2015 ER61 (PANSTARRS), the first instance of watching a long-period comet turn on. Pre-discovery observations and observations from the *NEOWISE* space telescope suggest that the nucleus is large, with a radius of $R_N \sim 9$ km, assuming an albedo of 0.025. Our photometric data follows the comet from $r = 8.9$ to 4.8 au as it moved into solar conjunction in 2016 July. Our sublimation model shows that activity began near $r = 8.8$ au (true anomaly, TA $= -139°$) in early 2015, driven by CO_2 sublimation, which peaked in 2016 April at $r = 5.1$ au (TA $= -127°$). Appreciable water sublimation began around $r = 5.0$ au. Our sublimation model is consistent with an active water sublimation area of 1% of the surface (equivalent to 10.2 km^2), and an active surface area for CO_2 sublimation of 0.029% (0.3 km^2). The CO_2 production rate at $r = 4.66$ au as measured by *NEOWISE* is $(8.4 \pm 2) \times 10^{25}$ s^{-1}. If CO_2-ice had been present on the surface, dust dragged from the surface by sublimation would have been observed much farther out—as far as 20 au. Our thermal models suggest that the CO_2 ice was present at a depth of 0.4 m. The comet came out of solar conjunction in 2016 December and, unless it brightens significantly, is unlikely to have water production rates much higher than a few $\times 10^{28}$ s^{-1}.

Key words: comets: general – comets: individual (C/2015 ER61) – methods: observational

1. Introduction

C/2015 ER61 was discovered by the Pan-STARRS1 telescope on 2015 March 14 as an apparent asteroidal object of mag $\sim$21. At the time, it was at $r = 8.45$ au from the Sun, $\Delta = 7.48$ au from the earth, a phase angle of $\alpha = 1°.4$, and at true anomaly, TA $= -138°.59$ was inbound. C/2015 ER61 is on a long-period (LP) comet orbit ($e = 0.9973$, $i = 6.3491°$, $q = 1.0421$ au, $Q = 771.2$ au; Epoch 2017 May 9.757201), but it is not dynamically new.[9] The comet will reach perihelion on 2017 May 9.77. Since this object initially appeared inactive and was on a long-period orbit, it met the criteria for a potential "Manx" comet. Manxes are inactive or nearly inactive objects coming in from the Oort cloud that may represent early inner solar system volatile-poor material that was ejected during the solar system formation (Meech et al. 2016).

If the discovery brightness estimate reflected a bare nucleus, the object was very large, with a radius between 13 and 19 km, assuming a range of typical comet albedos. Because of the possibility that C/2015 ER61 was a Manx object and because of its potentially large size, we undertook an observing campaign to characterize it. By 2015 June ($r = 7.7$ au), there was a faint coma visible in the images. After it came out of solar conjunction at the end of 2015, it was designated as a comet (see Figure 1).

Since late 2015, when the comet passed inside $r = 6$ au, the comet has brightened significantly and is no longer considered

a Manx object. The activity beyond this distance was not controlled by water-ice sublimation (Meech & Svoren 2004, pp. 317–335); the likely drivers are either CO or CO_2. This has presented a unique opportunity to watch the onset of sublimation in a long-period comet. The combination of a large nucleus and a small perihelion distance suggests that this comet could become intrinsically quite bright. Exceptionally bright (naked-eye visible) comets are rare, appearing only at a rate of about two per century (Meech 2017), and all have been LP comets. Conversely, until the recent advent of deep all-sky surveys, there have been no inactive or weakly active LP comets (Meech et al. 2016). Unfortunately, the geometry at perihelion makes it unlikely to become a naked-eye comet as seen from Earth.

With a perihelion distance of $q = 1.042$ au, this object is also classified as a near-Earth object (NEO). It has long been known that long-period comets that come close to the Earth present a particular hazard, their first approach allowing for little warning time. Without the well-developed tail at large heliocentric distance typical of long-period comets, an inactive object on such an orbit would be especially hazardous because it would be more difficult to detect.

2. Observations and Data Reduction

The data in this paper comprise the observing campaign we undertook using the facilities on Maunakea (Gemini North 8 m telescope, the Canada–France–Hawai'i (CFHT) 3.6 m telescope, and the University of Hawai'i 2.2 m telescope), the

---

[9] See Nakano Note: www.oaa.gr.jp/~oaacs/nk/nk3075.htm.
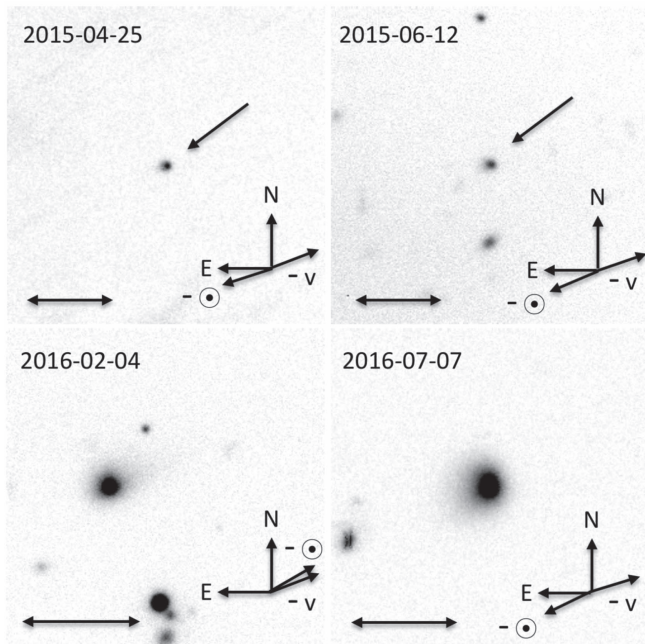
Figure 1. Sequence of images showing the appearance of C/2015 ER61 and its apparent lack of coma near $r \sim 8$ au in 2015 April. The coma is just visible as an eastward extension in 2015 June, and well developed by 2016 February. Scale bars show 50,000 km projected in the plane of the sky, and compass shows the direction to north, east, and the expected directions of the dust tail ($-v$, the negative of the heliocentric velocity vector) and gas tail ($-\odot$, the antisolar direction).

Himalayan *Chandra* 2 m Telescope in India, and the *WISE* space telescope. Additional data were obtained from the two survey telescopes in Hawai'i: Pan-STARRS1 and ATLAS. Archival data from the European Southern Observatory was also searched for any non-targeted observations of the comet. The circumstances of the observations are detailed below and summarized in Table 1. To obtain information about observing conditions for the runs executed in survey mode or via queue scheduling, we relied on both information in the image headers and data from the CFHT SkyProbe camera, which samples the atmospheric attenuation every minute by measuring the flux of a few hundred stars in the Tycho photometric catalog.

Finally, once the comet became brighter, we combined our measurements with data from the Minor Planet Center Electronic Circulars (MPEC) and two amateur comet observing sites.

2.1. Gemini North 8 m Telescope

We have a program to observe Manx objects using the Gemini North telescope in queue mode. However, for newly discovered objects, we rely on the new "Fast-Turnaround" program to secure time. We thus obtained the initial C/2015 ER61 data using our Manx program (GN-2016A-Q-15) and the subsequent data were obtained using the Fast-Turnaround (GN-2015A-FT-18). Data were obtained using the Gemini Multi-Object Spectrograph (GMOS) in imaging mode using the upgraded GMOS-N e2v DD devices. The detector was read out with pixels binned 2×2 with slow read (read noise = 3.32 e-) and low gain (2.27 e-/ADU).

2.2. Canada–France–Hawai'i Telescope (CFHT)

We obtained imaging data using the MegaPrime/MegaCam wide-field imager, an array of 40 2048 $\times$ 4612 pixel CCDs with a plate scale of 0.″187/pixel and 1° FOV. MegaCam is on the telescope for a period centered on each new moon, and data are obtained through queue service observing and are processed to remove the instrumental signature through the Elixir pipeline (Magnier & Cuillandre 2004).

2.3. University of Hawai'i Telescope (UH)

We observed remotely from Manoa on two nights using the UH 2.2 m telescope with the Tek2K CCD imaging camera and the Kron–Cousins filter system. This detector was read out in 1×1 binning mode resulting in a pixel scale of 0.″219/pixel with a gain of 1.78 e-/ADU and read noise of 30 e-.

2.4. Pan-STARRS1 (PS1)

Pan-STARRS1 (PS1) is a 1.8 m wide-field synoptic survey telescope on Haleakala with a 3°.2 $\times$ 3°.2 1.4 gigapixel camera (GPC1), consisting of a mosaic of 60 orthogonal transfer arrays, each comprising 64 590 $\times$ 598 pixel CCDs (Kaiser et al. 2002). The PS1 filter system is based on the SDSS survey, with some differences (Tonry et al. 2012). With a well-known orbit and a brightness estimated to be above the PS1 limiting magnitude prior to its discovery epoch, we conducted a search through the PS1 database for pre-discovery images. Images through the w_{P1} filter were found on three pre-discovery dates as shown in Table 1. Additional w_{P1} ($\lambda_{\mathrm{eff}} = 608$ nm, $\Delta\lambda = 382$ nm), r_{P1} ($\lambda_{\mathrm{eff}} = 617$ nm, $\Delta\lambda = 139$ nm), and z_{P1} ($\lambda_{\mathrm{eff}} = 866$ nm, $\Delta\lambda = 104$ nm) post-discovery images were also found.

2.5. ATLAS

The ATLAS telescope in Hawai'i (Tonry 2011) is an asteroid impact early warning system consisting of two 0.5 m telescopes that scan the entire sky visible in Hawai'i once every four nights. ATLAS-Haleakala has begun full operations and ATLAS-Mauna Loa will soon be operational. The completed production system will scan the entire visible sky every night, and will obtain accurate magnitudes on objects between *V* magnitude 20 and 9 in at least two broadband filters. At present, it can reach magnitudes as faint as $V \sim 19$. Data on C/2015 ER61 became available from ATLAS beginning in 2016 March, and are shown in Table 1.

2.6. Himalayan Chandra Telescope (HCT)

As part of our Manx characterization efforts, we have a long-term program on the 2.01 m HCT at Mt. Saraswati, Hanle India to obtain images for astrometry and heliocentric light curves. We used the Himalaya Faint Object Spectrograph and Camera (HFOSC) with the Bessell/Cousins filter system to obtain data on the two dates shown in Table 1. The detector has a read noise of 4.8 e- and gain of 1.22 e-/ADU and was read out in 1×1 binning mode with a pixel scale of 0.″296/pixel. This telescope cannot autoguide at non-sidereal rates, so we kept exposures short enough to keep trailing to less than the typical seeing while guiding at sidereal rates.

Table 1
Observation Log

UT Date	Tel	Instrum	Filter	#[a]	Exp[a] (s)	Sky[b]	Scale[c] ($''$ pix^{-1})	r[d] (au)	Δ[d] (au)	α[d] (°)	TA[d] (°)	Tail[e] (°)	r mag[f]
2014 Feb 12	VST	OmegaCam	i	4	960	CLR	0.210	11.332	10.387	1.54	−144.5	292.4	23.5 ± 0.3
2015 Jan 21	PS1	GPC1	w_{P1}	2	90	CLR	0.260	8.851	8.155	4.70	−139.6	292.3	22.27 ± 0.25
2015 Jan 23	PS1	GPC1	w_{P1}	1	45	CLR	0.260	8.836	8.117	4.55	−139.6	292.3	22.62 ± 0.39
2015 Feb 16	PS1	GPC1	w_{P1}	3	135	CLR	0.260	8.652	7.716	2.23	−139.1	292.8	21.49 ± 0.25
2015 Mar 15	PS1	GPC1	w_{P1}	4	180	CLR	0.260	8.441	7.470	1.53	−138.6	292.9	21.69 ± 0.24
2015 Apr 22	PS1	GPC1	w_{P1}	3	135	CLR	0.260	8.145	7.491	5.60	−137.8	292.1	21.46 ± 0.25
2016 Jan 08	PS1	GPC1	w_{P1}	4	180	CLR	0.260	5.938	5.602	9.19	−130.2	291.3	18.66 ± 0.17
2016 Jan 15	PS1	GPC1	z_{P1}	3	135	CLR	0.260	5.873	5.427	8.91	−129.9	291.5	18.59 ± 0.19
2016 Jan 16	PS1	GPC1	z_{P1}	2	90	CLR	0.260	5.864	5.403	8.55	−129.9	291.5	18.50 ± 0.20
2016 Jan 18	PS1	GPC1	w_{P1}	1	45	CLR	0.260	5.847	5.357	8.74	−129.8	291.6	18.47 ± 0.21
2016 Feb 02	PS1	GPC1	r_{P1}	4	180	CLR	0.260	5.710	5.014	7.47	−129.2	292.0	18.22 ± 0.18
2016 Feb 10	PS1	GPC1	r_{P1}	1	45	CLR	0.260	5.637	4.848	6.50	−128.2	292.2	18.01 ± 0.17
2016 Feb 19	PS1	GPC1	w_{P1}	4	180	CLR	0.260	5.554	4.679	5.18	−128.5	292.5	17.82 ± 0.20
2016 Apr 02	PS1	GPC1	w_{P1}	4	180	CLR	0.260	5.150	4.203	3.92	−126.4	292.9	17.06 ± 0.17
2015 Apr 16	UH	Tek2K	R	7	6300	cirrus	0.219	8.191	7.465	5.07	−137.9	292.3	21.246 ± 0.025
2015 Apr 24	CFHT	Megacam	gri	12	4800	cirrus	0.187	8.129	7.502	5.77	−137.7	292.0	21.070 ± 0.028
2015 Apr 25	CFHT	Megacam	$griz$	20	8000	cirrus	0.187	8.121	7.507	5.85	−137.7	292.0	21.212 ± 0.030
2015 Jun 01	VST	OmegaCam	i	5	1200		0.210	7.827	7.785	7.44	−136.9	290.1	20.935 ± 0.048
2015 Jun 12	Gemini	GMOS	$griz$	14	3800	CLR	0.146	7.735	7.879	7.38	−136.6	289.6	21.084 ± 0.022
2015 Jun 19	UH	Tek2K	R	2	1800	cirrus	0.219	7.678	7.934	7.23	−136.5	289.3	20.868 ± 0.057
2015 Dec 08	CFHT	Megacam	r	3	360	CLR	0.187	6.215	6.389	8.83	−131.3	290.7	19.153 ± 0.008
2016 Feb 02	CFHT	Megacam	r	6	1080	CLR	0.187	5.711	5.014	7.48	−129.2	292.0	18.209 ± 0.002
2016 Feb 04	Gemini	GMOS	$griz$	14	1285	CLR	0.146	5.692	4.972	7.25	−129.1	292.0	18.615 ± 0.005
2016 Apr 11	HCT	HFOSC	VR	6	900	CLR	0.296	5.061	4.175	5.83	−126.0	292.7	17.324 ± 0.009
2016 May 08	CFHT	Megacam	r	2	180	CLR	0.187	4.802	4.211	10.44	−124.5	291.2	16.998 ± 0.003
2016 May 31	HCT	HFOSC	R	1	400	CLR	0.296	4.571	4.330	12.71	−123.0	289.2	17.008 ± 0.010
2016 Jun 08	CFHT	Megacam	r	3	270	CLR	0.187	4.495	4.374	13.05	−122.5	288.6	16.862 ± 0.003
2016 Jul 07	CFHT	Megacam	r	3	60	CLR	0.187	4.201	4.524	12.70	−120.3	286.9	16.695 ± 0.003
2017 Jan 26	CFHT	Megacam	r	1	30	CLR	0.187	1.924	2.185	26.77	−85.3	275.0	14.466 ± 0.001
2015 Dec 23	*WISE*		$W1, W2$	13	100.1	N/A	1.0	6.080	6.014	9.31	−130.8	291.0	N/A
2016 May 25	*WISE*		$W1, W2$	11	84.7	N/A	1.0	4.634	4.294	12.28	−123.4	289.7	N/A
2016 Mar 05	ATLAS	STA-1600	cyan	4	120	CLR	1.86	5.413	4.446	2.58	−127.8	292.8	17.77 ± 0.05
2016 Mar 29	ATLAS	STA-1600	cyan	4	120	CLR	1.86	5.187	4.222	3.14	−126.6	293.0	17.22 ± 0.05
2016 Apr 02	ATLAS	STA-1600	cyan	4	120	CLR	1.86	5.149	4.202	3.96	−126.4	292.9	17.50 ± 0.05
2016 Apr 13	ATLAS	STA-1600	cyan	4	120	CLR	1.86	5.044	4.172	6.19	−125.9	292.7	17.47 ± 0.05
2016 Apr 15	ATLAS	STA-1600	cyan	4	120	CLR	1.86	5.025	4.170	6.58	−125.8	292.6	17.15 ± 0.05
2016 Apr 16	ATLAS	STA-1600	cyan	8	240	CLR	1.86	5.015	4.170	6.78	−125.7	292.5	17.07 ± 0.04
2016 Apr 21	ATLAS	STA-1600	cyan	4	120	CLR	1.86	4.966	4.170	7.73	−125.4	292.3	17.07 ± 0.05
2016 Apr 27	ATLAS	STA-1600	cyan	4	120	CLR	1.86	4.908	4.179	8.78	−125.1	292.0	17.10 ± 0.05
2016 Apr 29	ATLAS	STA-1600	cyan	4	120	CLR	1.86	4.889	4.183	9.11	−125.0	291.8	17.37 ± 0.05
2016 May 01	ATLAS	STA-1600	cyan	4	120	CLR	1.86	4.869	4.188	9.43	−124.9	291.7	17.40 ± 0.05
2016 May 03	ATLAS	STA-1600	cyan	4	120	CLR	1.86	4.850	4.194	9.73	−124.8	291.6	17.37 ± 0.05
2017 Feb 07	ATLAS	STA-1600	cyan	4	120	CLR	1.86	1.782	1.950	30.20	−80.3	271.6	14.28 ± 0.02

Notes.
[a] Total number of exposures and total exposure time [s].
[b] Sky conditions: CLR—clear, cirrus—less than ∼0.4 mag extinction, correctable with differential photometric calibration.
[c] Instrument pixel scale.
[d] Heliocentric, geocentric distances, phase angle, and True Anomaly.
[e] Estimated direction for the dust tail, PsAMV, from JPL Horizons.
[f] SDSS r-mag, converted from bandpass listed in this table (with the exception of nights with multiple filters, in which case only the filter closest to r was converted) as discussed in the text. The reported magnitude is the average for the night.

2.7. Neowise

The *NEOWISE* mission uses the reactivated *WISE* spacecraft, which began survey operations in 2013 December (Mainzer et al. 2014). Without any cryogens, only the two short-wavelength channels at 3.4 μm (*W1*) and 4.6 μm (*W2*) are available. Strong gas emission lines of CO (4.67 μm) and CO_2 (4.23 μm) fall within the *W2* band. While CO can be observed from the ground, CO_2 is only directly observable from space. The *NEOWISE* survey has covered the position of the comet during two visits, in 2015 December and 2016 May as shown in Figure 2.

2.8. Observatory Archives

We used the Solar System moving-Object Image Search tool (SSOIS) from the CADC (Gwyn et al. 2012) to search for any
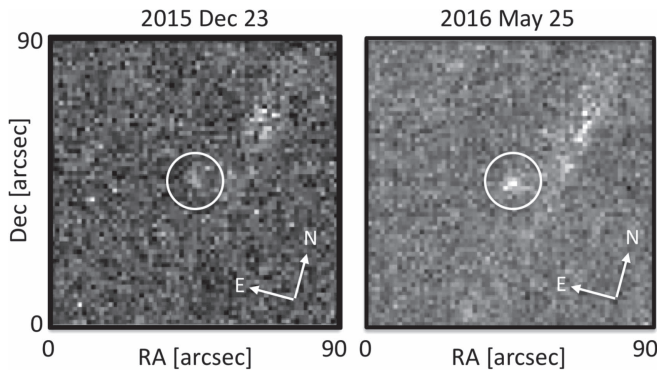
Figure 2. Images of comet C/2015 ER61 as observed by the *WISE* space telescope through the *W2* filter on 2015 December 23 and 2016 May 25. The comet is the faint source in the center of the image inside the circle.

frames in publically archived data that might have had pre-discovery data for C/2015 ER61. This search resulted in data covering the position of the comet on two dates obtained with the European Southern Observatory VLT Survey Telescope (VST; see Table 1). This 2.6 m telescope is equipped with OmegaCAM, a wide-field imager (1° × 1° deg). The comet was not seen in the earliest set of images, which were obtained ∼1 year prior to its discovery, but was detected, active, in the second set of images. The non-detection can be used to estimate the nucleus size (see Section 3.2).

2.9. Image Processing and Photometric Calibration

All of the optical imaging data except for PS1 and CFHT Megacam were flattened in a standard manner using our image reduction pipeline, and all data were calibrated using our calibration tools. The pipeline identifies image files by their instrument, and generalizes access to their widely varying metadata. The image reduction component bias-subtracts and flattens the data, and then applies the Terapix tools (Bertin & Arnouts 1996; Bertin 2006) to fit a precise World Coordinate System to the frame. PS1 and Megacam data were reduced by IPP (Kaiser et al. 2002) and Elixir (Magnier & Cuillandre 2004), respectively. The photometric calibration accesses the Pan-STARRS database (Magnier et al. 2013) or the Sloan Digital Sky Survey (SDSS, Fukugita et al. 1996; Doi et al. 2010) to provide a photometric zero point for each image, using published color corrections to translate photometric bands. Finally, the headers are used to identify the target and download orbital elements from the Minor Planet Center; the resulting object location is used to determine which object in the frame corresponds to the target. In the final pass, Terapix tools (SExtractor) are run to produce multi-aperture and automatic aperture target photometry. Given a directory of calibration images and object images from a known instrument with good pointing, we are thus able to produce a set of calibrated object magnitudes in a nearly automated manner.

For the nights where some cirrus was reported, we have found that the differential calibration to a large number of field stars recovers the brightness with no flux loss for extinctions up to 1 mag and that this is not color dependent. In particular, for 2015 April 25 for which we obtain a spectral reflectivity, the CFHT Skyprobe showed that for most of the data the extinction was <0.15 mag, and in no cases was it larger than 0.55 mag. Removing data for extinction larger than 0.15 mag did not

change the slope of the spectral reflectivity, giving us assurance that the technique is robust.

To convert the R (Cousins) system magnitudes to the SDSS-band r shown in Table 1, we used the transformations of Lupton,[10] where

$$r = R + 0.2936(r - i) + 0.1439. \tag{1}$$

The transformations from the PS1 filters to r are given by (Tonry et al. 2012)

$$r = w_{P1} - 0.018 - 0.118(g - r) + 0.091(g - r)^2 \tag{2}$$

$$r = r_{P1} - 0.001 + 0006(g - r) + 0.002(g - r)^2 \tag{3}$$

$$r = z_{P1} + (r - z) + 0.013 - 0.040(g - r)$$
$$+ 0.001(g - r)^2. \tag{4}$$

2.10. Colors and Spectral Reflectivity

The spectral reflectivity, R_λ, at each wavelength was computed relative to the g filter using the following equations

$$R_\lambda = \frac{10^{-0.4(f_\lambda - f_\odot)}}{10^{-0.4(g - g_\odot)}} = \frac{N}{D} \tag{5}$$

$$\sigma_{R\lambda} = R_\lambda^2 \left[\left(\frac{0.9212 N \sigma_\lambda}{N} \right)^2 + \left(\frac{0.9212 D \sigma_g}{D} \right)^2 \right]^{0.5}. \tag{6}$$

Here f_λ is the bandpass, σ_λ is the error on f_λ, and $f_\odot$ is the absolute magnitude of the Sun in that bandpass. We use $g_\odot = 5.12 \pm 0.02$ $r_\odot = 4.69 \pm 0.03$ $i_\odot = 4.57 \pm 0.03$ $z_\odot = 4.60 \pm 0.03$.

The colors derived from the photometry for the comet at three epochs are shown in Table 2, and the spectral reflectivity is shown in Figure 3. A linear fit to the reflectivity as a function of wavelength shows that at the first epoch (2015 April 25), the reflectivity, R obeys $R \propto (0.2250 \pm 0.1915)\lambda$ but at the second epoch (2015 June 12) $R \propto (0.7789 \pm 0.1382)\lambda$ and at the third epoch (2016 February 4) $R \propto (0.7934 \pm 0.1179)\lambda$. The disagreement between the first epoch and either the second or third epochs is at the 2.34 sigma level. The implications are discussed in Section 4.

3. Analysis and Results

3.1. Volatile Production Rates: CO and CO_2

We used the *NEOWISE* data to estimate the presence of CO or CO_2, which manifests as an excess flux above the dust signal in the *W2* bandpass. In order to estimate a volatile production rate from the excess flux, we remove the nuclear flux from the data, and establish a dust spectral energy distribution (SED; Bauer et al. 2011, 2015).

The *WISE* data have all been processed through the *WISE* science data pipeline (Wright et al. 2010) to bias subtract, flatten the images, and remove artifacts. The images are then stacked using the comet's apparent rate of motion (see Figure 2). In order to produce an SED, aperture photometry is converted to fluxes using the *WISE* zero points and appropriate color temperature corrections (Wright et al. 2010). These corrections are temperature dependent, and an initial guess at the temperature is required based on the expected black-body temperature for the heliocentric distance
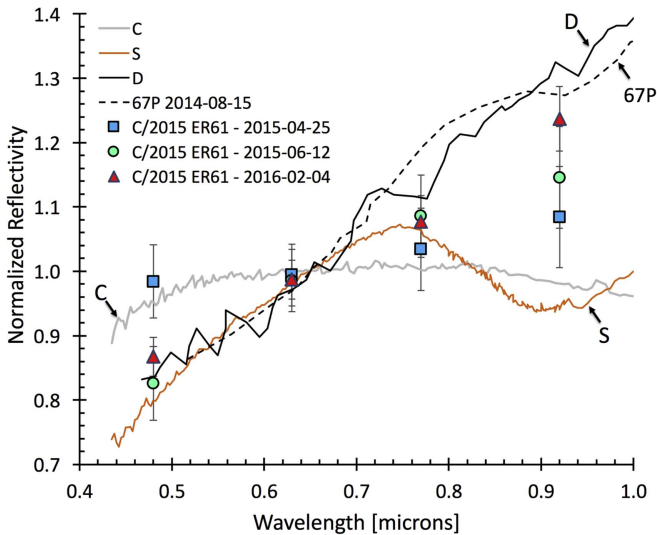
---

[10] http://classic.sdss.org/dr4/algorithms/sdssUBVRITransform.html#Lupton2005

Figure 3. Spectral reflectivity for C/2015 ER61 from three dates compared to asteroid spectral classes (Ceres, C; 32 Pomona, S; 1143 Odysseus, D; and comet 67P/Churyumov Gerasimenko). The asteroid data are from the SMASS survey (Bus & Binzel 2002), and the comet 67P/Churyumov-Gerasimenko spectrum is from Capaccioni et al. (2015). All data have been normalized to 1.0 at 0.65 μm.

Table 2
C/2015 ER61 Colors and Reflectivity

a†		Colors				
	$g - r$	σ_{g-r}	$r - i$	σ_{r-i}	$r - z$	σ_{r-z}
A	0.473	0.036	0.186	0.033	0.209	0.047
B	0.589	0.028	0.214	0.043	0.233	0.033
C	0.557	0.007	0.202	0.009	0.310	0.009

a†			Reflectivities				
	R_g	σ_{Rg}	R_r	σ_{Rr}	R_i	σ_{Ri}	R_z	σ_{Rz}
A	1.00	0.06	1.01	0.05	1.05	0.05	1.10	0.07
B	1.00	0.03	1.16	0.03	1.26	0.07	1.32	0.06
C	1.00	0.03	1.12	0.03	1.21	0.04	1.37	0.05

Note.
a† Date of run: A—2015 April 25, B—2015 June 15, C—2016 February 04.

of the observation. During the cryogenic mission, the two longest band passes ($W3$ and $W4$) are iteratively fit for temperature and color correction to derive the scaled Planck function until the solutions converge to within a few percent of each iteration. The current data were acquired during the warm mission, and we use a technique that has been modified by Reach et al. (2013) for the *Spitzer* warm mission to work with only the two shortest wavelength bands, $W1$ and $W2$.

The nucleus fluxes are derived from an estimated nucleus size using a NEATM thermal model with the beaming parameter near 1 (Bauer et al. 2015). The nucleus flux is then subtracted from the total flux at each wavelength. The reflected-light contribution is based on an assumed surface reflectance of 0.04 since the albedo of the particular object is unconstrained. We assume a particle size distribution with a power law that varies as a^{-3}, where a is the grain size (Fulle 2004). Typically the $W2$ excess is generally well above the dust contribution if CO/CO$_2$ is active. Because the 5%–10% band flux uncertainty dwarfs any uncertainty in the power-law index, this technique
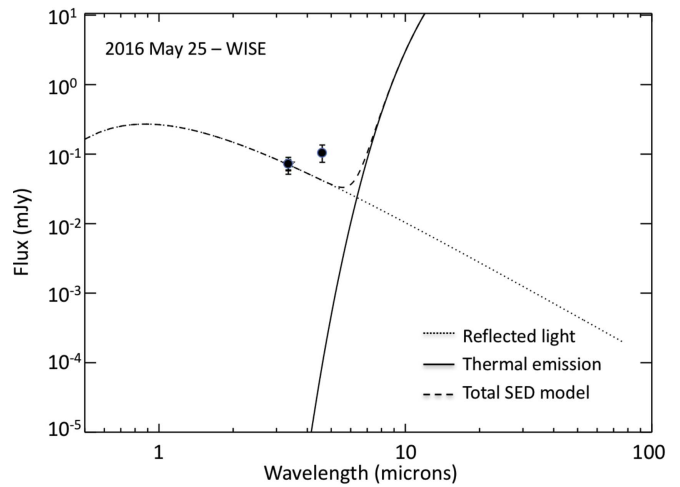

Figure 4. Spectral energy distribution (SED) for the 2016 May 25 *WISE* data showing the excess emission in the $W2$ band due to CO or CO$_2$ emission or a combination of the two.

Table 3
NEOWISE Volatile Production Rates

UT Date	r[a]	TA[b]	Q_{CO}[c]	Q_{CO2}[c]
2015 Dec 23	6.09	−130.82	$<1.2 \times 10^{27}$	$<1.1 \times 10^{26}$
2016 May 23	4.66	−123.56	$(8.9 \pm 2) \times 10^{26}$	$(8.4 \pm 2) \times 10^{25}$

Notes.
[a] Heliocentric distance [au].
[b] True Anomaly [deg].
[c] Predicted CO or CO$_2$ sublimation rate, molecules s^{-1}. Upper limits are 3σ.

is not strongly dependent on the dust size distribution slope. The SED fit to the data is shown in Figure 4.

The $W2$ band encompasses both the CO 1–0 and CO$_2$ ν_3 emission bands, making it difficult to separate their contributions. Because the ratio of the CO$_2$ to CO g-factors is $\sim$11.2 (Bockelee-Morvan & Crovisier 1989), a given flux would imply a much higher production rate for CO than CO$_2$. The values we obtain for the production rates for these species, assuming that it is either all CO or all CO$_2$ are shown in Table 3.

3.2. Nucleus Size Estimates

One of the challenges in characterizing LP comets is the difficulty in getting a nucleus size estimate, because by the time they are discovered they are very active. For this comet, we can use the non-detection on 2014 February 12 from the VST when the comet was at $r = 11.33$ au to place a limit on the nucleus size. A single image reaches S/N = 5 for mag $\sim$ 22 and S/N = 2.2 for mag $\sim$ 23. Thus the 5σ limiting magnitude in four exposures is about 23, and the 3σ limiting magnitude is $i \sim 23.3$. Assuming a typical 4% albedo (Li et al. 2013), this corresponds to an upper limit for the nucleus radius between 7 and 10 km.

We also use the estimates obtained from all of the PS1 data between 2015 January and 2015 April when there was no apparent coma, finding a range of possible sizes from 5.5–11.3 km given the errors on the photometry.

The December *WISE* $W1$-band magnitude was 18.6 ± 0.4. Assuming a typical color of $V–W1 = 1.6$, and assuming a 0.7 mag correction for phase, and using the techniques

described above (Section 3.1) this results in a radius of $R_N \sim 10.8 \pm 2.1$ km, which is consistent with the determination above. Given it was slightly active in 2015 December, we place more weight on the PS1/VST data.

Combining all of these consistent estimates, we adopt a radius of 9 km as the input parameter for use in the sublimation models discussed below.

3.3. Conceptual Ice Sublimation Model

We used a simplified ice sublimation model to investigate the level of activity versus heliocentric distance. The model computes the amount of gas sublimating from an icy surface exposed to solar heating (Cowan & A'Hearn 1982; Meech et al. 1986; Meech & Svoren 2004, pp. 317–335). As the ice sublimates, either from the nucleus surface or near-subsurface, the escaping gas entrains dust in the flow, which escapes into the coma and tail. The scattered brightness of the comet as measured from Earth has a contribution from the light scattered from the nucleus and the dust. Model free parameters include the ice type, nucleus radius, albedo, emissivity, density, dust properties (sizes, density, phase function), and fractional active area.

The total coma brightness, m_{coma}, can be expressed as a function of the mass loss [dM/dt] via

$$m_{\mathrm{coma}} = 30.7 - 2.5 \log_{10}\left[\frac{p_g(dM/dt)t}{a_g\rho_g r^2 \Delta^2}\right] \quad (7)$$

where p_g is the grain albedo, a_g and ρ_g are the grain radius and density, and r and Δ are the heliocentric and geocentric distances. The time t is a function of the projected aperture size and grain velocity (approximated for small grains well coupled to the gas as the Bobrovnikoff velocity (Delsemme 1982, pp. 85–130): $v \sim 0.5\ r^{-0.5}\,\mathrm{km\,s^{-1}}$ for r in au).

The mass loss is computed using the energy balance at the nucleus:

$$F_\odot(1 - A)/r^2 = \chi\left[\epsilon\sigma T^4 + L(T)\frac{dm_s}{dt} + \kappa\frac{dT}{dz}\right]. \quad (8)$$

The left-hand side of the equation is the absorbed solar flux and the terms on the right-hand side represent the black-body energy, the energy going into sublimation, and conduction into the interior. χ is a rotation parameter expressing whether the nucleus is isothermal. The mass loss per unit area, (dm_s/dt) is related to the sublimation vapor pressure and the average molecular gas speed. The sources for the latent heats $L(T)$ and sublimation vapor pressures for some common ices are summarized in Meech et al. (1986).

We assume a nucleus radius of $R_N = 9$ km (as determined previously in Section 3.2), a nucleus and dust albedo of 0.04, and a linear phase function of 0.04 mag deg^{-1} for the nucleus typical of other comets. The albedo is based on the observed range of average comet surface albedos from spacecraft, ranging between 0.04–0.07 (Li et al. 2013; Ciarniello et al. 2015). We use a shallower phase function of 0.02 mag deg^{-1} for the dust (Krasnopolsky et al. 1987; Meech & Jewitt 1987). We assume that the nucleus density can range between 400 and 600 kg m^{-3} as seen from recent in situ missions (Thomas et al. 2013a, 2013b; Jorda et al. 2016). We assume an average bulk grain density of 1000 kg m^{-3}, and a range of grain sizes dominated on the small end by submicron to micron-size grains

Table 4
Sublimation Model Parameters

Parameter	Initial	Best Fit
Radius [km]	9	
Emissivity, ϵ	0.9	
Phase function [mag/deg], β_{nuc}	0.04	
Phase function [mag/deg], β_{coma}	0.02	
Grain density [kg m^{-3}], ρ_{grain}	1000	
Nucleus density [kg m^{-3}], ρ_{nuc}	400–600	400
Albedo, p_v	0.04	0.025
Grain size [μm], a_{grain}	0.1–10	5
Active Area [%], f_{H2O}	4	1
Active Area [%], f_{CO2}	0	0.029

as seen from ground-based observations and results from the Rosetta mission (Yang et al. 2014; Fulle et al. 2016).

Because of the many model free parameters, our conclusions are dependent on our ability to constrain some of the values with observations. The shape of the light curve—where the curve is steep or shallow—is constrained by the sublimating ice composition. With reasonable estimates of nucleus size, albedo, density, and grain properties, the fractional active surface area is adjusted to reproduce the observed volatile production rates. We initially assumed only water-ice sublimation. Table 4 shows the initial parameters in the middle column, and the best final fit for the parameters that were allowed to vary in the right-hand column.

Figure 5 shows all of the data reported in Table 1 in addition to data from the MPECs and two amateur sites with well-calibrated data: the Comet OBServation Database (COBS)[11] and the Spanish comet light curve website.[12] These data were normalized to account for the different aperture sizes to the data in Table 1 by shifting the sets so that the locus of the amateur data matched our data when there was overlap. For the COBS and Spanish data, we selected aperture sizes that were closest to the 5 arcsec radius that we report in Table 1. The larger scatter in the MPEC data reflects unknown aperture sizes.

The data and model are shown in Figure 5. We found that with the nominal nucleus radius, we had to lower the albedo to get the curve to fit the data (or equivalently, we could have reduced the nucleus radius to 7.2 km). The short dashed curve in Figure 5 is the brightness of the nucleus, which is constrained to be consistent with the VST non-detection and the earliest PS1 data points. Figure 5 shows that the comet began to develop a dust coma near TA = −140°, i.e., between 8–9 au. At this distance from the Sun, it is too cold for water-ice sublimation to be effective. Both CO and CO_2 are good candidates for activity beyond 6 au (TA $\sim$ −130°). However, if either volatile were on the surface, the sublimation would have been strong and the comet would have been very active by 9 au. For CO_2, the nucleus would be actively sublimating well beyond 10 au and beyond 30 au for CO, creating the large tail typical of active LP comets. This did not occur, suggesting that these volatiles were well below the surface. An insulating porous dust layer (or perhaps a water ice layer as seen during the Rosetta mission (Biele et al. 2015; Gulkis et al. 2015)) caused a delay in the arrival of the solar energy to the ice layer.

---

[11] www.cobs.si
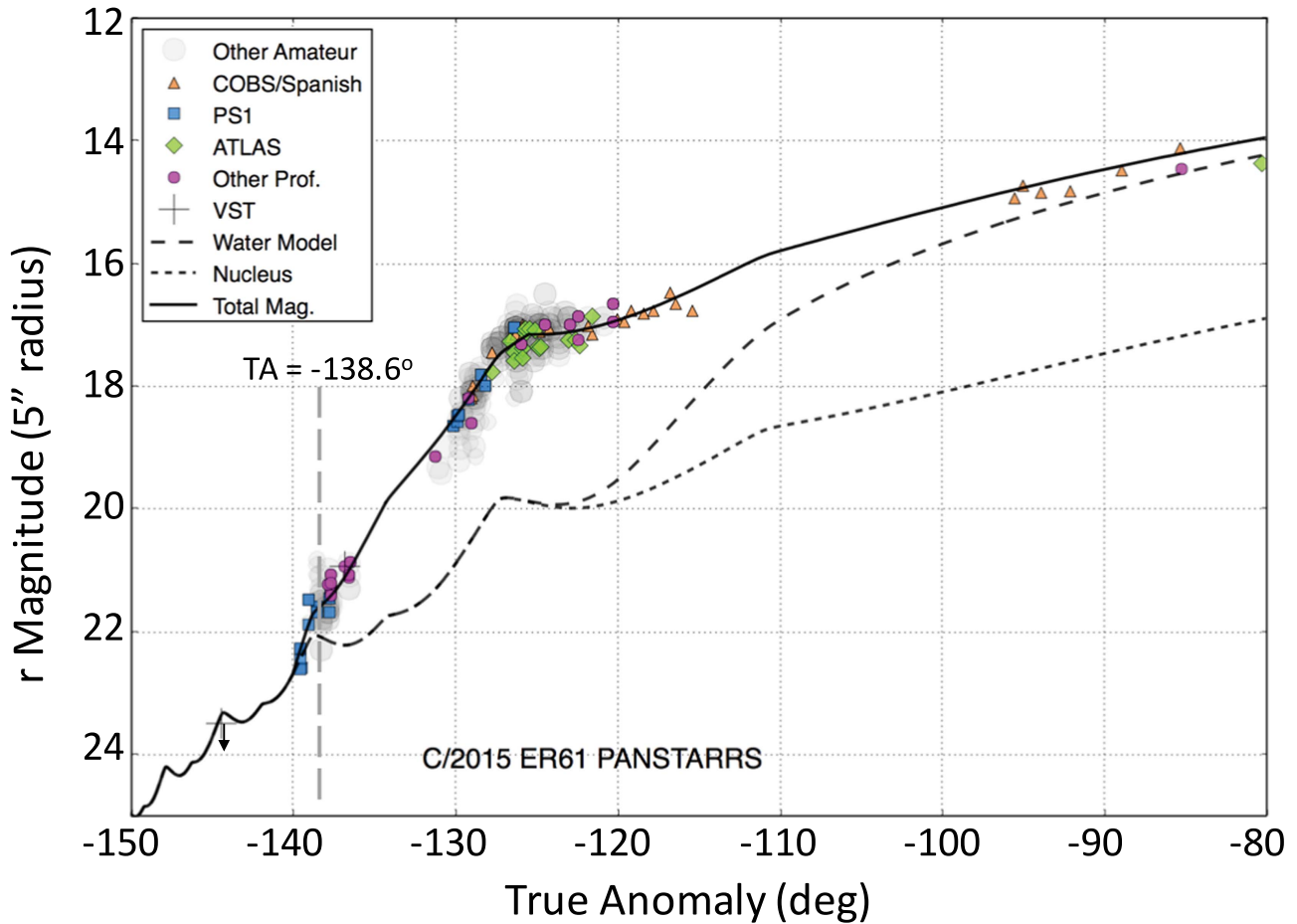[12] http://www.astrosurf.com/cometas-obs.

Figure 5. Comparison of professional (Gemini, CFHT, UH, HCT, VST), PS1 and ATLAS survey, and amateur data (COBS and spanish group) for C/2015 ER61. The latter were obtained with the same photometric apertures, greatly reducing the scatter. MPC data are shown as the gray cloud. All data have been normalized to match the data from the large telescopes. The heavy black curve shows the total model brightness incorporating contributions from both H_2O and CO_2 sublimation. The vertical gray line at TA $= -138°.6$ shows the discovery epoch.

We simulate this in the model as delay in heat reaching the depth of the ice, modeled by an exponential curve and as constrained by the observed volatile production rates shown in Table 3. The model shown in Figure 5 combines CO_2 and H_2O sublimation. The CO_2 production peaked near TA $= -125°$ (near $r \sim 5$ au) and then fell off linearly, indicating a depletion of the source region. We can also fit for CO, but without other constraints (e.g., detection of CO or limits on its production from ground-based observations), we cannot distinguish between the CO or CO_2. It is more likely that CO_2 is driving this activity based on insights we have seen from recent space missions (A'Hearn et al. 2012). The best-fit parameters for H_2O and CO_2 are shown in Table 4.

Because many of the free parameters are coupled, calibrating this model requires ground-based measurements of water production rates.

3.4. Thermal Modeling

The ice sublimation model described above provides an estimate of the amount of volatiles emerging from the comet as a function of heliocentric distance, but does not estimate the depth from which they emerge. We employ two thermal modeling techniques to assess the depth for these volatiles.

If CO or CO_2 were present on the surface, there would be gas flux sufficient to drag enough dust from the surface to cause an observable increase in the comet brightness to detect activity from the heliocentric light curve at much larger heliocentric distances. For example, using $\Delta m = 0.05$ mag as the detection criterion, activity from surface CO_2 sublimation would be detectable near $r \sim 20$ au (TA $\sim -153°.8$, $V \sim 25.9$). The date at which the turn on actually happened gives a time delay and this can be used to solve the 1D heat conduction equation to find the depth:

$$\frac{\partial T}{\partial t} = k \frac{\partial^2 T}{\partial z^2} \tag{9}$$

$$k = \frac{I^2}{\rho^2 c_p}. \tag{10}$$

Here k is the thermal conductivity, I is the thermal inertia, and c_p is the heat capacity. We use the value in Table 4 for the nucleus density, and $c_p = 500 \, \mathrm{J \, kg^{-1} \, K^{-1}}$ as determined from the Rosetta mission (Alií-Lagoa et al. 2015). A range of thermal inertias have been reported from Rosetta $10 < I < 50 \, \mathrm{J \, K^{-1} \, m^{-2} \, s^{-0.5}}$ (Gulkis et al. 2015), which are consistent with those reported for the Deep Impact and Stardust-NExT missions (Groussin et al. 2013).

To solve this equation, the outer boundary condition was set to the equilibrium surface temperature, T_{eq}, at the comet's

current distance from the Sun determined by

$$T_{eq} = T_\odot (1 - p_v)^{\frac{1}{4}} \sqrt{\frac{R_\odot}{2r}} \qquad (11)$$

where $T_\odot$ and $R_\odot$ are the temperature and radius of the Sun. The inner boundary condition was set to below 80 K for CO_2, with the inner boundary significantly deeper in the comet than in the ice, and thus was expected to avoid boundary effects. The differential equation was solved with steps of 0.1 day from 1969 to 2015 with steps of 0.02 m down to a depth of 20 m. The arbitrary integration start date was chosen at a time when the comet would be so far from the Sun that it would be too cold for surface CO_2-ice sublimation. The results for the CO_2 ice depth are $d = 0.54, 1.10, 1.65, 2.2, 2.75$ m for thermal inertias of $I = 10, 20, 30, 40, 50$ J K^{-1} m^{-2} s$^{-0.5}$, respectively.

In order to explore the onset of activity in more detail, our second method used a simple thermophysical model to estimate the subsurface depth of CO or CO_2 ice, which is believed to be the driver of activity beginning around TA = $-140°$. This model uses a simplified version of the equations derived by Prialnik et al. (2004, pp. 359–387). The 1D heat equation is used to solve for the radial temperature profile of the nucleus interior assuming it is non-rotating and spherical. The heat equation, solving for the temperature profile, is given by

$$\frac{\partial T}{\partial t} = \alpha \frac{\partial^2 T}{\partial z^2} - \frac{1}{c_p \rho} \sum_i q_i \mathcal{H}_i \qquad (12)$$

where $\alpha = k/(c_p \rho)$ is the thermal diffusivity, k is the thermal conductivity, c_p is the heat capacity, and ρ is the density of each layer. The thermal conductivity and heat capacity are functions of the composition, temperature, and porosity of each layer ($k(n_i, T, \Psi)$ and $c_p(n_i, T, \Psi)$). Their relations are derived from empirical formulas found in Huebner et al. (2006). The second term on the right-hand side describes the heat loss due to sublimation from each layer. The volume sublimation rate of each species is given by

$$q_i = \text{SVR}(\Psi, r_p)\left[(\mathcal{P}_i - P_i)\sqrt{\frac{m_i}{2\pi kT}}\right] \qquad (13)$$

where SVR is the surface-to-volume ratio of the porous medium, $\mathcal{P}(T)$ is the saturation vapor pressure of the species, and $P(T)$ is the partial pressure of the gas in the pore space of the layer. The SVR was modeled similarly to the treatment of a distribution of cylindrical capillaries found in Prialnik et al. (2004, pp. 359–387) and Sarid et al. (2005). Gas pressures and the change in enthalpy due to sublimation, $\mathcal{H}$, were calculated using empirical formulas from Huebner et al. (2006). The surface boundary condition is given by equating energy balance at the surface of the nucleus,

$$(1 - A)\frac{L_\odot}{4\pi r^2} = \epsilon \sigma T^4 + \sum_i \mathcal{F}_i \mathcal{P}_i \sqrt{\frac{m_i}{2\pi kT}} \mathcal{H}_i \qquad (14)$$

where solar energy input, black-body emission of the nucleus, and heat loss due to sublimation at the surface are included. Here $A = 0.012$ is the bond albedo, derived from an assumed geometric albedo of 0.04, $L_\odot$ is the solar constant, $\epsilon = 0.95$ is the emissivity, and the fraction of surface area containing the i-th ice species is $\mathcal{F}_i$.

Mass loss due to volatile sublimation was included in the model by calculating the sublimation rate of the three volatile species (H_2O, CO, and CO_2) for each interior layer at the end of every time step. The sublimation rate was assumed to be constant during each time step, which allowed a total amount of sublimated material to be calculated. This amount of material was then subtracted from the compositional mass fractions of the layers. Gas flow through the porous comet material was ignored for this simple model. Any material released through sublimation was assumed to be emitted from the nucleus.

A Crank–Nicolson method was used for solving the partial differential equation. Layer sizes on the order of millimeters were used near the surface where large temperature gradients are expected. Thermal evolution of the nucleus starts with the comet at its aphelion distance. The following equations are used to simulate the orbit of the comet and are in terms of the eccentric anomaly (E):

$$t = \sqrt{\frac{a^3}{G M_\odot}} (E - e \sin E) \qquad (15)$$

$$r = a(1 - e \cos E). \qquad (16)$$

To model the depth of CO or CO_2 ices at TA = $-140°$, we thermally evolved a progenitor nucleus, initially homogeneous in composition, for 100 complete orbits. The orbital parameters used for C/2015 ER61 came from the JPL Small-Body Browser. The initial composition of each layer was chosen to be 47% crystalline water ice ($H_2O)_c$, 0.02% CO ice, 0.01% CO_2 ice, and 50% dust by volume. Additionally, the model uses an initial porosity of 70% (from recent *Rosetta* results from comet 67P (Taylor et al. 2015)), which is allowed to evolve in each layer due to the loss of material from sublimation. Mass loss due to dust emission and surface recession is ignored in this model. While these values may not reflect actual compositional abundances for the nucleus, the values were chosen to reflect approximate values found for other comet nuclei.

Our goal of finding the approximate depths for CO or CO_2 ice does not rely heavily on the abundances used during modeling. To more accurately determine measurements for the composition of the nucleus, production rates from the modeling would need to be fit to observational production rates, which is beyond the scope of this simple modeling exercise. Furthermore, at the time of modeling, there were no water production rates yet available.

Figure 6(A) shows the evolution of the radial temperature profile seen for the first and tenth orbits of C/2015 ER61. The temperature profile at TA = $-140°$ (near the time of discovery at TA = $-138°.6$) is used for estimating the depth for CO or CO_2 ice (Figure 6(B)). At the tenth orbit, CO and CO_2 were depleted down to depths of 6.9 m and 0.4 m, respectively. It is sublimation of these buried volatiles that is believed to cause the increased activity seen at this time. To estimate the depths of both ices, the depth at which the temperature profile reaches a certain threshold temperature is used for the ice depth. A value of 25K for CO and 80K for CO_2 ice was used (Meech & Svoren 2004, pp. 317–335).

The radial temperature profile evolution and the radial temperature profile for an orbital position of TA = $-140°$ reach a near steady state after the first few orbits (Figure 6(C)). This is a reflection of the simplification where we are not incorporating a mechanism for dust mass loss and surface recession. Although the temperature profile reaches a steady
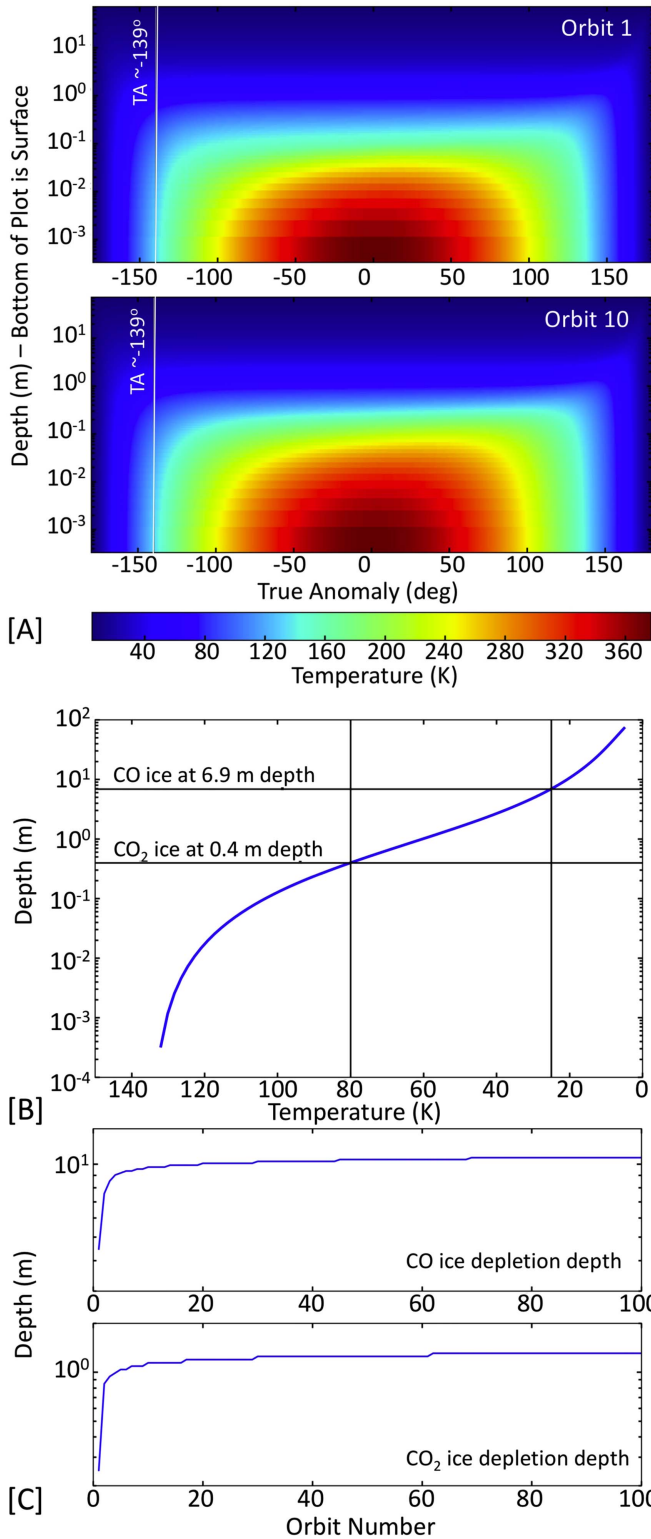
[A]

[B]

[C]

Figure 6. (A) Temperature evolution of the radial profile for orbits 1 and 10 for C/2015 ER61. The vertical marker at TA = −139° indicates the time of discovery and corresponds to the radial profile shown in part B. A thermal wave is seen to propagate into the interior of the nucleus, which can drive sublimation from interior layers. (B) Radial temperature profile for orbit 10 at TA = −140°, showing the depth to the CO and CO_2 ice layers. The depths have increased slightly from 6.3 and 0.38 m in orbit 1. (C) CO and CO_2 ice recession during the 100-orbit model. The depth shown for each orbit indicates the depth at which the abundance of volatile species has reached 0% for TA = −140°.
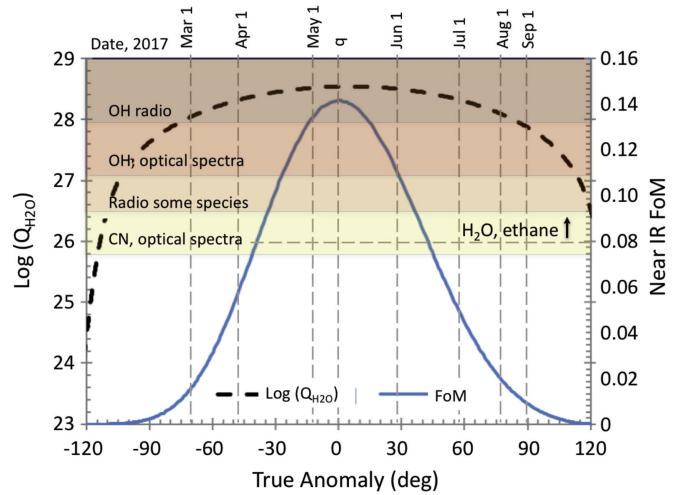
Figure 7. Best-fit model water production rate, Q_{H2O} (dashed curve) and near-IR figure of merit (FoM, solid curve) vs. position along the orbit, where True Anomaly = 0° is at perihelion on 2017 May 9). The shaded regions show the approximate water production rates required to detect water and other species using various techniques (Crovisier et al. 2002; Mumma et al. 2002; Crovisier et al. 2009; Meech et al. 2011b), and the horizontal dashed line shows when the near-IR FoM is high enough to start to detect water.

state at this early stage, there is still a modificaiton of the interior layer's ice abundances throughout the full 100 orbits modeled.

4. Discussion

Our ice sublimation model can represent cometary activity for the three most abundant volatile ices (H_2O, CO, CO_2) over the comet's orbit (Meech et al. 1986; Meech & Svoren 2004, pp. 317–335). As a comet approaches the Sun, incident solar radiation warms the surface; when there is sufficient energy, the ices sublimate, dust is dragged from the nucleus, increasing the comet's scattering cross section. A comet's heliocentric light curve can provide information about what major volatiles are present, and in what relative amounts and when they contribute to the activity. When combined with independent measurements of the production rates of key volatiles, the models are tightly constrained. This approach has been successful in predicting the relative volatile abundances in comet 103P/ Hartley 2 (Meech et al. 2011a), the onset of activity in comet C/2012 S1 (ISON) (Meech et al. 2013), and the general activity level and distance at which the *Rosetta* instruments would first begin to detect water for comet 67P/Churyumov-Gerasimenko (Snodgrass et al. 2013). However, for a detailed understanding of the physical processes in the nucleus, sophisticated thermophysical models are needed.

Our sublimation model showed further that the CO or CO_2 was coming from depth beneath the surface and solving the 1D heat conduction equation suggests that the depth is around 0.5 m for CO_2 based on the delayed onset of activity. This was consistent with the more detailed thermophysical model presented in Section 3.4 which showed that CO ice would be at a depth of 6.9 m and CO_2 ice at a shallower depth of 0.4 m. It is interesting to note that the simple models give a similar result to the more sophisticated thermophysical model with variable thermal inertia. This was not this comet's first passage through the inner solar system, so one would not expect the more

volatile ices to be at the surface. Had the CO_2 been on the surface, there would have been possible brightening as dust was lifted off as far out as 20 au (TA $\sim -153°$, early in 2010).

The model fit presented in Figure 5 is constrained using the CO_2 production rate measured by *NEOWISE* (assuming the detection was all CO_2, however, without measurements constraining CO production, we cannot say which volatile controls the activity at large r. The fit is additionally constrained with an H_2O production rate of $Q(H_2O) = 1.5 \times 10^{28}$ molec s^{-1} measured with the TRAPPIST telescope on 2017 February 10−11 (E. Jehin 2017, private communication) and $Q(H_2O) = 1.9 \times 10^{28}$ measured from Nançay radio telescope between 2017 February 8–25 (J. Crovisier, private communication). Figure 7 shows the estimates for the water production rates, $Q(H_2O)$, for the current best-fit model. Also plotted is the near-IR figure of merit (FoM; Mumma et al. 2002), a measure of the water spectral line brightness at IR wavelengths when water release is controlled only by insolation. This is determined by FoM $= Q\, r^{-1.5}\, \Delta^{-1} \times 10^{-29}$. Unless the comet has a significant increase in brightness near perihelion, this model predicts that the comet will be relatively faint for near-IR high-resolution spectroscopy.

It is interesting to note the apparent change in spectral reflectivity as seen in Figure 3, where the reflectivity reddened from 2015 April to June and later. During 2015 April, while there was some activity, it was still very low, little dust was seen, and the reflectivity was less red. In-situ observations during the Rosetta encounter with comet 67P/Churyumov-Gerasimenko showed significant color changes on the nucleus surface. This was in response to water that sublimated when the surface was in sunlight having frozen in the surface layers after sunset. The presence of surface frosts changed the spectral reflectivity of the surface, making it appear locally much bluer (Fornasier et al. 2015). Likewise, the most active regions had bluer slopes, where more surface ice was exposed (Fornasier et al. 2015). The southern hemisphere of 67P inbound was also not as red, not having seen sunlight until near perihelion. It is possible that the apparent color change seen in Figure 3 indicates a nucleus surface that had either condensed water-ice frost on the outbound leg, or which had much of the dust removed from perihelion.

During 2015 April, when the comet was at $r = 8.1$ au, the lifetime of micron-sized grains or thin frost layers can be longer than 10^{10} s for pure water ice; however, with even just 10% amorphous carbon, the lifetime would be only ~ 1 month. Thus, it is reasonable that the comet could have undergone a surface color change in the ~ 1.5 months between observations.

Since coming out of solar conjunction, the comet will be visible as a morning object for up to two hours through perihelion. However, because the geocentric distance will be 1.24 au at perihelion it will not be spectacularly bright. The comet will remain observable until it goes into solar conjunction again in 2018 April at $r = 4.5$ au. After that, there is good visibility every year for many years between about August and May.

We presented the first, direct observations of the onset of activity of a long-period comet, at a heliocentric distance near 8.8 au; a simple sublimation model indicates this was caused by the sublimation of subsurface CO or CO_2 ice. Additional data around perihelion, and molecular production rates will further constrain the models.

The reddening of the object's reflectivity during its first months of activity, and the depletion of ice from the surface layer give independent suggestions that this object is not on its first orbit from the Oort cloud.

References

A'Hearn, M. F., Feaga, L., Keller, H. U., et al. 2012, ApJ, 758, 29
Alí-Lagoa, V., Delbo, M., & Libourel, G. 2015, ApJL, 810, L22
Bauer, J. M., Stevenson, R., Kramer, E., et al. 2015, ApJ, 814, 85
Bauer, J. M., Walker, R. G., Mainzer, A. K., et al. 2011, ApJ, 738, 171
Bertin, E. 2006, in ASP Conf. Ser. 351, Automatic astrometric and photometric calibration with SCAMP, ed. C. Gabriel, C. Arviset, & S. Enrique (San Francisco, CA: ASP), 112

Bertin, E., & Arnouts, S. 1996, A&AS, 117, 393
Biele, J., Ulamec, S., Maibaum, M., et al. 2015, Sci, 349, aaa9816
Bockelee-Morvan, D., & Crovisier, J. 1989, A&A, 216, 278
Bottke, W. F., Durda, D. D., Nesvorný, D., et al. 2005, Icar, 179, 63
Bus, S. J., & Binzel, R. P. 2002, Icar, 158, 106
Capaccioni, F., Coradini, A., Filacchione, G., et al. 2015, Sci, 347, aaa0628
Ciarniello, M., Capaccioni, F., Filacchione, G., et al. 2015, A&A, 583
    A31
Crovisier, J., Biver, N., Bockelee-Morvan, D., & Colom, P. 2009, P&SS,
    57, 1162
Cowan, J. J., & A'Hearn, M. F. 1982, Icar, 50, 53
Crovisier, J., Colom, P., Gerard, E., Bockelee-Morvan, D., & Bourgois, G.
    2002, A&A, 393, 1053
Delsemme, A. H. 1982, in Comets, ed. L. L. Wilkening (Tucson, AZ: Univ.
    Arizona Press), 85
Denneau, L., Jedicke, R., Grav, T., et al. 2013, PASP, 125, 357
Doi, M., Tanaka, M., Fukugita, M., et al. 2010, AJ, 139, 1628
Finson, M. L., & Probstein, R. F. 1968, ApJ, 154, 353
Fornasier, S., Hasselmann, P. H., Barucci, M. A., et al. 2015, A&A, 583
    A30
Fornasier, S., Mottola, S., Keller, H. U., et al. 2016, Sci, 354, 1566
Fukugita, M., Ichikawa, T., Gunn, J. E., et al. 1996, AJ, 111, 1748
Fulle, M. 2004, in Comets II, ed. M. C. Festou et al. (Tucson, AZ: Univ.
    Arizona Press), 565
Fulle, M., Marzari, F., Della Corte, V., et al. 2016, ApJ, 821, 19
Groussin, O., sunshine, J. M., Feaga, L. M., et al. 2013, Icar, 222, 580
Gulkis, S., Allen, M., von Allmen, P., et al. 2015, Sci, 347, aaa0709
Gwyn, S. D. J., Hill, N., & Kavelaars, J. J. 2012, PASP, 124, 579
Huebner, W. F., Benkhoff, J., Capria, M.-T., et al. 2006, Heat and gas diffusion
    in comet nuclei, ISSI Scientific Report, SR-004
Jorda, L., Gaskell, R., Caparra, C., et al. 2016, Icar, 277, 257
Kaiser, N., Aussel, H., Burke, B. E., et al. 2002, Proc. SPIE, 4826, 154

Krasnopolsky, V. A., Moroz, V. I., Krysko, A. A., Tkachuk, A. Y., &
    Moreels, G. 1987, A&A, 187, 707
Li, J.-Y., Besse, S., A'Hearn, M. F., et al. 2013, Icar, 222, 559
Magnier, E. A., & Cuillandre, J.-C. 2004, PASP, 116, 449
Magnier, E. A., Schlafly, E., Finkbeiner, D., et al. 2013, ApJS, 204, 20
Mainzer, A., Bauer, J., Cutri, R. M., et al. 2014, ApJ, 792, 30
Meech, K. J. 2017, RSPTA, in press
Meech, K. J., A'Hearn, M. F., Adams, J. A., et al. 2011a, ApJL, 734, L1
Meech, K. J., Jewitt, D., & Ricker, G. R. 1986, Icar, 66, 561
Meech, K. J., & Jewitt, D. C. 1987, A&A, 187, 585
Meech, K. J., Pittichova, J., Yang, B., et al. 2011b, Icar, 213, 323
Meech, K. J., & Svoren, J. 2004, in Comets II, ed. M. C. Festou et al. (Tucson,
    AZ: Univ. Arizona Press), 317
Meech, K. J., Yang, B., Kleyna, J., et al. 2013, ApJL, 776, L20
Meech, K. J., Yang, B., Kleyna, J., et al. 2016, SciA, 2, e1600038
Mumma, M. J., Disanti, M. A., dello Russo, N., et al. 2002, in Proc. of Asteroids,
    Comets, Meteors, ed. Barbara Warmbein (Noordwijk: ESA), 753
Prialnik, D., Benkoff, J., & Podolak, M. 2004, in Comets II, ed. M. C. Festou
    et al. (Tucson, AZ: Univ. Arizona Press), 359
Reach, W. T., Kelley, M. S., & Vaubaillon, J. 2013, Icar, 226, 777
Sarid, G., Prialnik, D., Meech, K. J., Pittichova, J., & Farnham, T. L. 2005,
    PASP, 117, 796
Schlafly, E. F., Finkbeiner, D. P., Jurić, M., et al. 2012, ApJ, 756, 158
Snodgrass, C., Tubiana, C., Bramich, D. M., et al. 2013, A&A, 557, A33
Taylor, M. G. G. T., Alexander, C., Altobelli, N., et al. 2015, Sci, 347, 387
Thomas, P., A'Hearn, M. F., Belton, M. J. S., et al. 2013a, Icar, 222, 453
Thomas, P., A'Hearn, M. F., Veverka, J., et al. 2013b, Icar, 222, 550
Tonry, J. L. 2011, PASP, 123, 58
Tonry, J. L., Stubbs, C. W., Lykke, K. R., et al. 2012, ApJ, 750, 99
Wright, E. L., Eisenhardt, P. R. M., Mainzer, A. K., et al. 2010, AJ, 140, 1868
Yang, B., Keane, J., Meech, K., Owen, T., & Wainscoat, R. 2014, ApJL,
    784, L23